### Title
Intermittent Lagrangian velocities and accelerations in three-dimensional porous medium flow




### Journal
Physical Review E, 92(1)

### ISSN
2470-0045



### Authors
Holzner, M
Morales, VL
Willmann, M
et al.



### Publication Date
2015-07-01

### DOI
10.1103/physreve.92.013015

Peer reviewed

# Intermittent Lagrangian velocities and accelerations in three-dimensional porous medium flow

M. Holzner*
*Institute of Environmental Engineering, ETH Zurich, Wolfgang-Pauli-Strasse 15, 8093 Zürich, Switzerland*

V. L. Morales
*SIMBIOS Centre, University of Abertay, Bell Street Dundee DD1 1HG, United Kingdom*

M. Willmann
*Institute of Environmental Engineering, ETH Zurich, Wolfgang-Pauli-Strasse 15, 8093 Zurich, Switzerland*

M. Dentz
*Spanish National Research Council (IDAEA-CSIC), c/Jordi Girona 18, 08034 Barcelona, Spain*
(Received 5 December 2014; published 17 July 2015)

Intermittency of Lagrangian velocity and acceleration is a key to understanding transport in complex systems ranging from fluid turbulence to flow in porous media. High-resolution optical particle tracking in a three-dimensional (3D) porous medium provides detailed 3D information on Lagrangian velocities and accelerations. We find sharp transitions close to pore throats, and low flow variability in the pore bodies, which gives rise to stretched exponential Lagrangian velocity and acceleration distributions characterized by a sharp peak at low velocity, superlinear evolution of particle dispersion, and double-peak behavior in the propagators. The velocity distribution is quantified in terms of pore geometry and flow connectivity, which forms the basis for a continuous-time random-walk model that sheds light on the observed Lagrangian flow and transport behaviors.

DOI: 10.1103/PhysRevE.92.013015 PACS number(s): 47.56.+r

## I. INTRODUCTION

Intermittency of Lagrangian velocities and accelerations plays an important role in the understanding of transport in complex systems such as fluid turbulence [1–3], flow in porous media [4,5], or animal locomotion [6,7]. While in turbulence and animal motion, intermittency is caused by the characteristic spectrum of turbulent eddies and animal behavior, respectively, in porous media it arises due to the confined and complex pore space in which flow occurs. Continuum models of porous media [8] are based on the validity of the Darcy equation for fluid and Fick's law for scalar fluxes on a representative elementary volume.

Fluctuations of pore-scale flow and scalar transport are averaged out and represented in terms of effective parameters such as hydrodynamic dispersion. However, the intermittent behavior of pore-scale flow impacts on the nature of particle and scalar transport, and it determines the way dissolved substances mix and react. The understanding of the origin of these processes is of both fundamental and practical importance in applications ranging from reactive transport in groundwater flow to diffusion in fuel cells or biological systems [9–11]. For engineered and natural porous media, they determine the mixing and dispersion of contaminants [12,13], biofilm growth, or the kinetics of chemical reactions [14–16]. On a fundamental level, pore-scale fluctuations may propagate to the continuum scale in a form that cannot be quantified by effective parameters [17], and they give rise to non-Fickian transport behaviors [18,19]. The qualitative and quantitative understanding of such collective phenomena requires an understanding of the physical origins of pore-scale flow fluctuations and intermittency.

Advancements in experimental techniques have allowed for a leap in our understanding of transport in turbulent flows by analysis of the Lagrangian properties of acceleration [20,21]. However, analogous measurements in porous medium flow have been hindered by the difficulty of probing flow through a complex solid pore matrix in three dimensions, and at fine enough resolutions to detect intense gradients. Most optical experimental measurements, such as particle image velocimetry, provide Eulerian velocity information limited to one or two velocity components [22–26]. Nuclear magnetic resonance (NMR) measurements provide three-dimensional (3D) flow information in real soil packings [15,27,28], and they have measured a broad range of proton displacements. Recent work by Datta *et al.* [29] characterized the flow field from empirical Eulerian measurements to understand the spatial structure of the flow. Their findings present a correspondence between velocity fluctuations with the shape of the pore space, which demonstrates that flow velocity is organized by the geometry of the porous medium. The statistics of velocity fluctuations from an Eulerian velocity field, however, cannot capture the features of intermittency, which requires Lagrangian data instead. De Anna *et al.* [4] probed the flow through a 2D porous medium in greater detail by studying pore-scale flow simulations within a Lagrangian framework. Evaluation of fluid particle displacements revealed superdiffusive dispersion, while the analysis of Lagrangian velocities and accelerations displayed persistent zones of stagnation and correlations that decay quickly for acceleration but slowly for velocity. Despite its importance for pore-scale transport, mixing, and reaction processes, little is known about intermittent flow organization with respect to the 3D

*holzner@ifu.baug.ethz.ch

 

pore-space geometry or the structural features of the porous medium that cause it.

In this work, we employ an experimental 3D particle tracking method that has been adapted to measure the flow velocity and accelerations along Lagrangian trajectories at high spatiotemporal resolution. Measurements are performed in a transparent porous medium that mimics the structure of sandy soil. Intermittent behavior of velocity and acceleration is observed and related to the succession of wide and narrow pore spaces along preferential flow channels. The strongest velocity and accelerations appear abruptly in the vicinity of pore throats, while in pore bodies the flow is nearly stagnant and velocities vary gradually. This double structure of the flow leads to anomalous transport as a consequence of the broad range of velocities and accelerations experienced by advected flow particles. To understand these behaviors, we develop a pore velocity model that accounts for pore geometry and connectivity, and we set up a continuous-time random walk (CTRW) for the Lagrangian velocity and particle transitions.

## II. EXPERIMENTAL SETUP

A transparent acrylic flow cell of size $3.8 \times 3.8 \times 3.8$ cm$^3$ was custom-built for the three-dimensional particle tracking velocimetry (3D-PTV) setup to allow illumination from the side by monochromatic light (Ar-ion laser) and stereoscopic viewing from the front (Fig. 1). Two sizes of Nafion grains (Ion power, Inc., New Castle, DE, and Walther G. Grot, Rockland, DE) of $d_1 = 3.7$ mm and $d_2 = 0.5$ mm were mixed and used as the transparent porous medium at a v/v ratio of 95/5, respectively. Nafion grains were allowed to become fully hydrated in the working 42 v/v % isopropanol aqueous solution for a minimum of 24 h in order to achieve a stable grain size. The flow cell was then packed wet with the hydrated Nafion until no additional grains fit through the cell opening. Full saturation was maintained in the cell during 3D-PTV measurements, and excellent matching of the index of refraction between solid phase and liquid was achieved (Fig. 2). The constant volumetric flow rate is 19 mL/min, the Darcy velocity is $q = 0.22$ mm/s, and the average interstitial pore velocity is $v_p = q/\phi = 0.95$ mm/s. The Reynolds number is $\mathrm{Re} = qd_1/\nu \simeq 0.4$, well within the valid range for Darcy's law ($\mathrm{Re} \leqslant 10$). An advective time scale can be defined as $t_A = d_1/v_p = 3.7$ s.

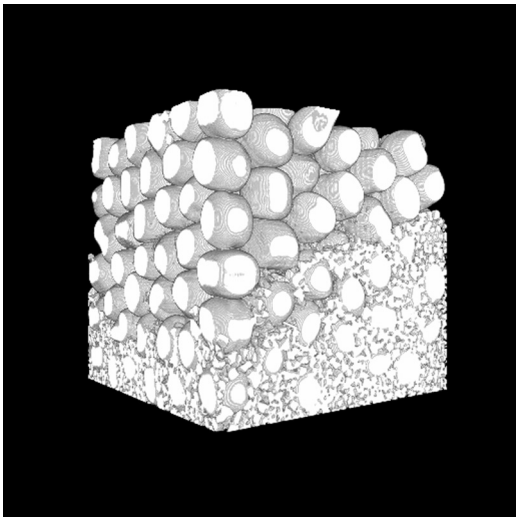

FIG. 1. Volumetric information obtained from x-ray computed tomography scanning of the Nafion grain-packed flow-through cell after 3D-PTV measurements. The flow-through cell has been cut away to show the sample interior, where white grains are the two sizes of Nafion. The tomographic image has cubic voxels of 50 $\mu$m in size.

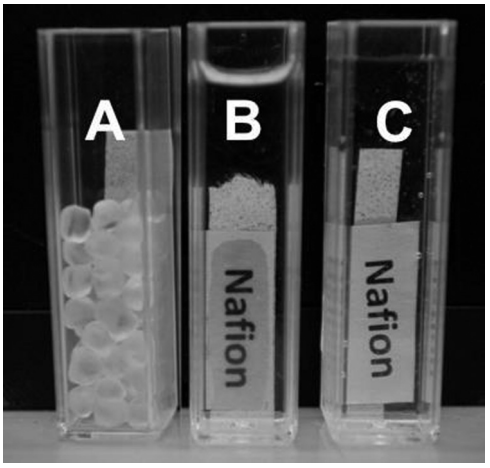


FIG. 2. Nafion grains (a), liquid saturated Nafion grains in isopropanol-water (b), and pure water (c).

### A. Particle tracking velocimetry

The liquid is seeded with neutrally buoyant fluorescent tracer particles with a diameter of 60 $\mu$m with a volume fraction concentration of 0.01%. The suspension is hence very dilute, and hydrodynamic interactions between tracer particles are negligible. The Stokes number of the particles (defined as the ratio between particle response time $t_p = 2.7 \times 10^{-7}$ s and advective time scale $t_A$) is $O(10^{-7})$, i.e., inertia effects are negligible. The size of the polystyrene tracer particles is about eight times smaller than the smaller grain diameter $d_2$ used for the experiments. Reference [30] showed that finite-size particles may sample the porous medium flow selectively. Large particles are transported faster through constricted regions since their center of mass is farther away from the matrix surfaces. Also, they observed that large particles cannot access the entire region between obstacles. As a consequence, they found major deviations in the average pore velocity measured from particle tracking. In our measurements, the difference between the pore velocity calculated from the measured flow rate and the average pore velocity measured from tracer particles was less than 10%. We have carried out additional experiments using silver-coated tracer particles with a size of 15 $\mu$m, i.e., 30 times smaller than $d_2$, and we did not observe significant differences in the results. We therefore concluded that finite-size effects were not significant.

For the optical 3D particle tracking measurements, we employ an Ar-ion laser to illuminate the particles, and a Photron high-speed camera with a resolution of $1024 \times 1024$ pixels, operated at a frame rate of 50 Hz and equipped with a four-way image splitter that mimics a multicamera setup [31].

About 500 particles are tracked per frame for a duration of 4 min.

The measurement accuracy in the 2D views $(x,y)$ is about 5 $\mu$m. The image splitter setup has several advantages (e.g., no need to synchronize), but the disadvantage is that it has a relatively large error of about 250 $\mu$m in the reconstruction of the raw $z$-coordinate of the trajectories. Following Lüthi *et al.* (2005), a Savitzky-Golay filter was applied for smoothing in time along Lagrangian trajectories, using a cubic polynomial fitted to 21 frames. After filtering, the accuracy can be calculated by 250 $\mu$m/(filter size/sampling rate)$^{1/2}$ = 55 $\mu$m. Components of Lagrangian velocity $u_i$ and accelerations $a_i$ $(i = x,y,z)$, as well as the components $\epsilon_{ij} = \partial u_i/\partial x_j$ of the Lagrangian deformation rate tensor and its symmetric part $s_{ij} = (\epsilon_{ij} + \epsilon_{ji})/2$, which is the rate of the strain tensor, are computed [32,33]. We compute the Lagrangian acceleration by differentiating the velocity along particle trajectories. The strain rate is denoted by $\mathcal{S} = \sqrt{\sum_{ij} s_{ij} s_{ij}}$. Average flow is along the positive $x$ direction, while $y$ and $z$ are the cross-sectional coordinates.

### B. X-ray computed tomography and topologic/geometric information of the pore space

Microtomography was used to nondestructively characterize the structure of the transparent porous medium used during particle tracking. X-ray computed tomography (XCT) images were thresholded and analyzed to determine the sample porosity, investigate the topology of the pore space, and extract the pore-size distribution. The method established by Pérez-Reche *et al.* [34] was followed for this sample. Briefly, this involves the following steps. First, the reconstructed XCT scans are cropped and segmented to generate image stacks that contain voxels corresponding only to the pore and porous medium of the sample (illustrated in Fig. 1). From the thresholded images, it is possible to quantify the porosity of the sample directly ($\phi = 0.23$). Next, the stacks are subjected to a thinning process, which extracts the medial lines of the pore space. Medial lines are subsequently differentiated between nodes and edges of the network equivalent of the pore space, and the topology is established accordingly. The pore-size distribution is computed from local measurements of the channel size along the length of the medial lines. More specifically, the local channel size is computed as the distance between a point on the medial line and the nearest grain boundary, which represents the radius of the smallest inscribed sphere that fits and is centered at that point on the network. Diameter equivalents are used for reporting mean pore size ($\langle S \rangle = 0.23$ mm) and pore-size distributions.

## III. EXPERIMENTAL OBSERVATIONS

Figures 3(a) and 3(b) show the logarithm of the velocity magnitude $\ln(|\mathbf{u}|)$ along Lagrangian trajectories in a portion of the observation volume. It is apparent that preferential flow paths develop where the velocity is high next to regions where velocities are much lower. The two magnified views of a high activity region show the velocity $u_x$ [Fig. 3(c)] and acceleration $a_x$ [Fig. 3(d)] components normalized by their standard deviations $\sigma_u$ and $\sigma_a$. It is illustrated how

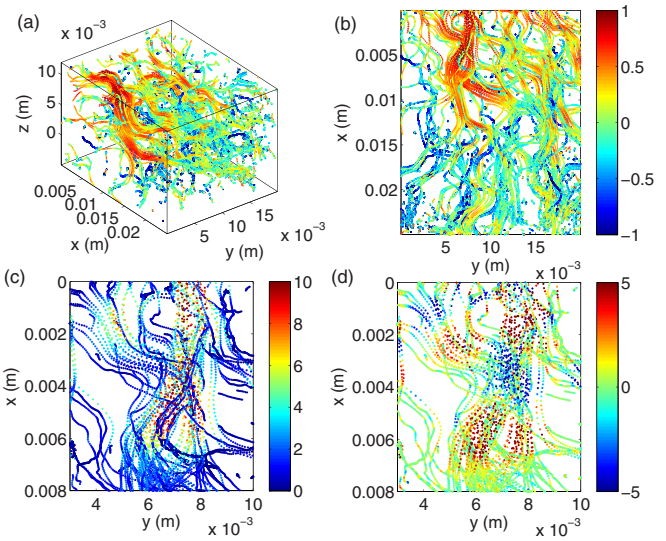


FIG. 3. (Color online) Three- (a) and two-dimensional (b) views of the logarithm of the velocity magnitude $\log(|\mathbf{u}|)$ normalized by its standard deviation along Lagrangian trajectories that are longer than 200 frames in a portion of the observation volume. Magnified views of the velocity $u_x$ (c) and acceleration $a_x$ (d) components normalized by their standard deviations.

intense velocities are reached in narrow pore throats where the trajectories converge. Here, accelerations are strong and change sign in correspondence to the relative maxima of velocity.

The probability density functions (PDFs) of longitudinal and transverse velocity components normalized by their standard deviations $\sigma$ are shown in Fig. 4(a). While the PDF of velocity in turbulent flow is typically of Gaussian shape, our measurements show that flow in a porous medium produces velocity PDFs with strongly non-Gaussian tails. The longitudinal velocity component has a peak near zero, and it has a strong positive and a weaker negative tail related to the occurrence of reversed flow. The transverse velocity components are slightly skewed, which is presumably related to finite-size effects or small anisotropic regions. We note that

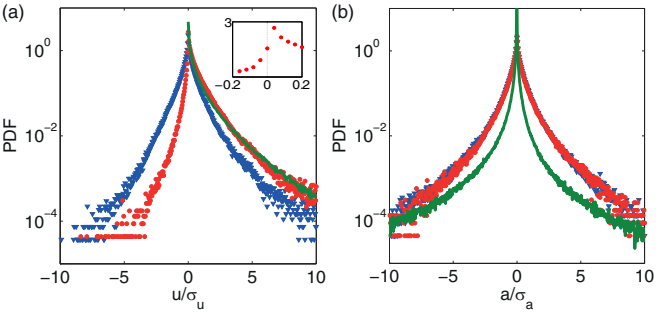


FIG. 4. (Color online) PDFs of longitudinal (circles, red) and transverse (triangles, blue) Lagrangian velocity (a) and acceleration (b) components normalized by their standard deviations $\sigma$ from experiment. Longitudinal velocity (a) and acceleration (b) from CTRW model (green line). The inset shows a closeup near zero of the longitudinal velocity component.

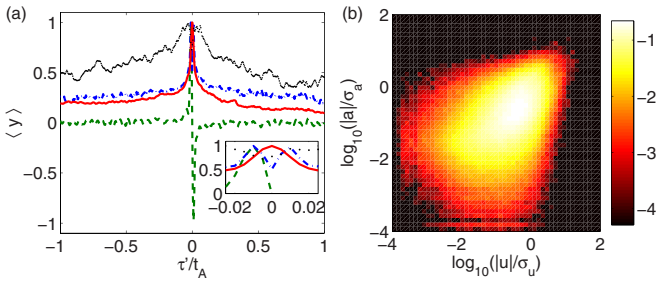


FIG. 5. (Color online) (a) Conditionally averaged Lagrangian evolution of $u_x$ (solid), $a_x$ (dashed), ($|\mathbf{a}|$) (dash-dotted), and $\mathcal{S}$ (dotted). The inset is a closeup at the origin. (b) Joint PDF of $|u_x|$ and $|a_x|$.

the velocity PDF can be represented by a stretched exponential model, consistent with simulations in stochastically generated geometries [35]. Velocity PDFs with broad tails but simple exponential decay were observed in experiments in bead packs [27–29] and 2D simulations of a medium composed of disks [36].

Measurements of the distributions of accelerations are shown in Fig. 4(b), which illustrates the PDFs of longitudinal and transverse accelerations normalized by their standard deviations $\sigma_a$. The PDFs of both acceleration components follow a stretched exponential shape and overlap, i.e., they do not exhibit the features of anisotropy. Their shape is similar to that of the velocity PDF [Fig. 4(a)], and it resembles typical acceleration PDFs in turbulent flow [20,21]. This points to a possible universal character of the distribution of acceleration that is shared among different correlated fluid flows [20].

The intermittent and interdependent attributes of Lagrangian velocity and acceleration in a porous medium flow can be understood qualitatively from Figs. 3(c) and 3(d). Fast and strong acceleration events coincide with high velocities localized in pore throats, while acceleration events are weak in pore bodies characterized by almost stagnant velocities. As a consequence, Lagrangian velocities and accelerations, which are sampled equidistantly in time along the particle trajectories, display sharp peaks at low magnitudes (Fig. 4). This interdependence can be illustrated more quantitatively by considering the conditional averages $\langle \mathcal{Y}(t') \rangle = \langle \mathcal{Y}(t - t_m) \rangle$ for $\mathcal{Y} = u_x$, $a_x$, $|\mathbf{a}|$, and $\mathcal{S}$, where $t_m$ is the time at which $u_x$ assumes a global maximum along the measured trajectory, and the angular brackets denote the average over all particle trajectories. Both velocity and acceleration rise steeply and show sharp (double) peaks around $t' = 0$ [Fig. 5(a)]. The longitudinal acceleration component reaches a positive peak shortly before $t' = 0$, followed by a rapid change to a negative peak of similar magnitude shortly after. Accordingly, the acceleration magnitude shows a positive double peak around the origin [inset of Fig. 5(a)]. Since flow converges in front of pore throats, fluid elements are strongly stretched in the longitudinal direction, which is manifested in the rise of the strain rate [Fig. 5(a)]. While a local minimum is observed at $t' = 0$ [inset of Fig. 5(a)], the highest stretching is reached before the maximum velocity, which is qualitatively similar to laminar flow through an orifice. This shows that strong events of velocity and acceleration occur at pore throats where fluid elements are exposed to high strain.

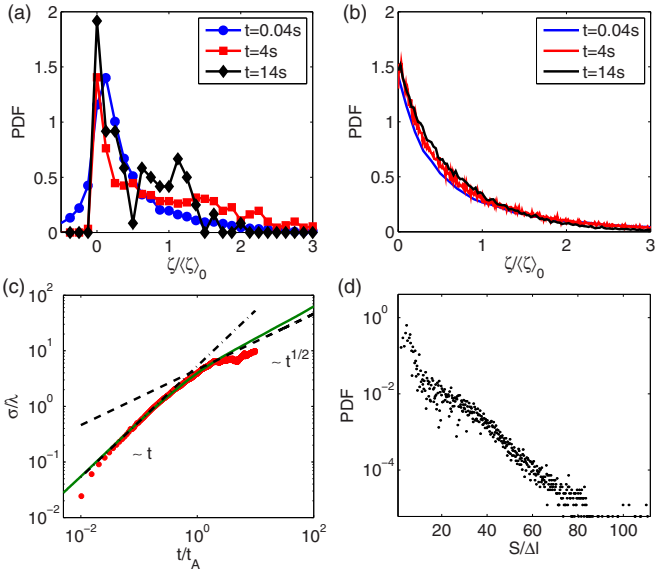


FIG. 6. (Color online) PDF of propagators $\zeta$ of advected tracer particle locations at various displacement times in experiment (a) and model (b). $\langle \zeta \rangle_0 = v_p t$ is the expected nominal mean displacement. Root-mean-square displacement from data (symbols) and CTRW model (solid line), superdiffusive scaling (dot-dashed line), Fickian scaling (dashed line) (c) and pore size PDF extracted from XRCT scan, voxel size $\Delta l = 50\ \mu$m (d).

The joint PDF of $|u_x|$ and $|a_x|$ shows that mid to high values have a moderate degree of pointwise correlation [Fig. 5(b)]. That is, when velocity is high, accelerations are also moderate to high and particles accelerate and decelerate strongly. A correlation, albeit weaker, is still present at low values of velocity and acceleration [also visible in Fig. 5(a)]. Low velocities are persistent and commonly exposed to low accelerations, but they feature a finite probability of moderate accelerations [Fig. 5(b)]. We find that this high variability of velocity and accelerations leads to anomalous dispersive behavior. Propagators of advected tracer particle locations are characterized by a strong stagnant peak present throughout the investigated time period, and a smaller secondary mobile peak that develops at time $t \geqslant 10$ s and moves at average flow speed [Fig. 6(a)]. We hence note that preasymptotic transport behavior and Fickian transport are not reached within an observation time of $O(10)t_A$ and a distance of $O(10)d_1$. Analogous observations of non-Fickian transport have been made in complex pore structures using NMR [37] and, more recently, using numerical simulations [38]. The root-mean-square displacement of particles features a ballistic behavior initially, before it transitions toward a possible superdiffusive regime [Fig. 6(c)]. In the following, we explore the quantification of these observations in terms of the pore geometry and flow structure. Toward that end, we develop a model for the PDF of pore velocities and set up a simple physically based correlated CTRW model [4,5,39].

## IV. STRETCHED EXPONENTIAL VELOCITY PDF

Note that flow through a single pore can be approximated by a parabolic profile characteristic of Poiseuille flow through a

pipe, $v(r) = v_m(1 - r^2/r_p^2)$, with $v_m$ the maximum velocity in the pore and $r_p$ the pore radius. Sampling this profile uniformly in space gives rise to the flat velocity PDF $p_v(v|v_m) = v_m^{-1}$ for $0 \leqslant v \leqslant v_m$ for a given maximum velocity $v_m$. The unconditional PDF of pore velocities is then given by

$$p_v(v) = \int_v^\infty dv_m v_m^{-1} p_m(v_m), \tag{1}$$

where $p_m(v_m)$ is the PDF of maximum pore velocities to be determined in the following. We note that for an arrangement of parallel, noninteracting pores with variable radius, the maximum pore velocity $v_m$ is determined by the constant pressure drop and the pore radius $r_p$ such that $v_m \propto (r_p/r_0)^2$, with $r_0$ a characteristic pore radius. For a serial arrangement, $v_m$ is determined by the constant total flux and the pore radius such that $v_m \propto (r_p/r_0)^{-2}$. For a connected pore network, we conjecture the dependence of $v_m$ on the pore radius according to the power law

$$v_m = v_0(r_p/r_0)^\alpha, \quad -2 \leqslant \alpha \leqslant 2 \tag{2}$$

with $v_0$ representing a characteristic pore velocity. The exponent $\alpha$ may be understood as a connectivity parameter that informs on the pore network geometry. As shown in Fig. 6(d), the distribution of pore radii $r_p$ can be well approximated by the exponential PDF $p_r(r_p) = \exp(-r_p/r_0)/r_0$. Combining the latter with (2) gives the stretched exponential PDF of maximum pore velocities, $p_m(v_m)$,

$$p_m(v_m) = v_0^{-1}(v_m/v_0)^{1/\alpha - 1} \exp[-(v_m/v_0)^{1/\alpha}]. \tag{3}$$

From (1), we then obtain the PDF of pore velocities,

$$p_v(v) = v_0^{-1}\Gamma[1 - \alpha, (v/v_0)^{1/\alpha}], \tag{4}$$

where $\Gamma(\alpha, v)$ is the incomplete Gamma function [40]. The characteristic velocity $v_0$ is given in terms of the mean pore velocity $\langle v \rangle = v_p$ as $v_0 = 2v_p/\Gamma(1 + \alpha)$. For small velocities $v \ll v_0$, $p_v(v)$ goes toward the constant $v_0^{-1}\Gamma(1 - \alpha)$, while for large $v \gg v_0$ it shows the stretched exponential behavior $p_v(v) \sim v_0^{-1} \exp[-(v/v_0)^{1/\alpha}]$. Notably, this velocity model explains the stretched exponential tail observed in the PDF of Lagrangian velocities in a series of pore-scale studies [35,41] by the exponential distribution of pore radii and the connectivity exponent $\alpha$ in (2).

## V. CONTINUOUS-TIME RANDOM WALK

The velocity PDF (4) is used in the framework of a CTRW model for particle displacements along the direction of the mean pressure gradient. This approach models particle movements as a random walk in space-time,

$$x_{n+1} = x_n + \ell_n, \quad t_{n+1} = t_n + \tau_n. \tag{5}$$

The path segment of length $\ell$ follows the distribution of pore length $p_\ell(\ell)$. The transition time $\tau_n$ between turning points is determined from the mean velocity along the segment $\overline{v}_n = (v_{n+1} + v_n)/2$ as $\tau_n = \ell/\overline{v}_n$. The velocities $v_n$ at the turning points $x_n$ of the CTRW are distributed according to $p_v(v)$ given by (4). The persistence of particle velocities in subsequent CTRW steps is modeled by a simple correlation model, which assigns a probability $\lambda$ to stay at the same velocity or $1 - \lambda$ to change it at the turning point. Particle positions $x(t)$ at time $t$ are given by linear interpolation of the positions at the turning points according to $x(t) = x_{n_t} + \overline{v}_{n_t}(t - t_{n_t})$, where $n_t$ is the renewal process $n_t = \max(n|t_n \leqslant t)$. The longitudinal Lagrangian particle velocities are then given by $u_x = \overline{v}_{n_t}$. The average particle acceleration between turning points is measured by $a_n = (v_{n+1} - v_n)/\tau_n$. Accordingly, longitudinal particle accelerations are given by $a_x = a_{n_t}$. In the following, we set the connectivity parameter $\alpha = 3/2$ and $v_0 = 2v_p/\Gamma(1 + \alpha)$ to parametrize the velocity PDF (4). The distribution of pore length is exponential with the characteristic length $\ell_0 = d/4$. The persistence of subsequent particle velocities is quantified by $\lambda = 9/10$.

This CTRW model quantifies quite well the PDF of Lagrangian velocities [Fig. 4(a)]. The peak at small velocities is captured by the CTRW in a natural way because particles spend more time in low-velocity regions as quantified by the transition time $\tau_n = \ell/\overline{v}_n$. The acceleration PDF from CTRW captures the measured behavior qualitatively but not quantitatively [Fig. 4(b)]. We would not expect that the CTRW model posed above can resolve the acceleration PDF because it operates on a coarse scale (the scale of a pore), and it cannot capture subpore velocity fluctuations. The particle propagators illustrated in Fig. 6(a) are qualitatively well described by the CTRW model [Fig. 6(b)]. The CTRW results are of the same order of magnitude and display a similar scaling behavior with $\langle \zeta \rangle_0$, which is the expected nominal mean displacement, as the experimental data. The double-peak behavior at late times cannot be captured by the present CTRW approach because it does not represent persistence of low- and high-velocity classes, which would be necessary to model such behavior. The evolution of particle dispersion is well captured by the CTRW model, both the ballistic short-time behavior as well as the onset of a possible superdiffusive regime [Fig. 6(c), solid line].

## VI. SUMMARY

In conclusion, our results show that flow in a soil-like porous medium is characterized by strongly intermittent velocity and acceleration. This establishes a connection between flow in porous media and turbulent flows that sheds light on the understanding of the universal nature of complexity [42] in hierarchical flow systems. The experimental analysis elucidates the interdependence between Lagrangian velocity, acceleration, and strain. Moreover, it is revealed that a double structure of flow localizes extreme events of low and high activity in the vicinity of pore throats and pore bodies. This double structure leads to anomalous dispersion, and it produces non-Gaussian velocity and acceleration PDFs characterized by strong peaks that correspond to the origin and stretched exponential tails. These features can be related to the pore-size distribution and flow connectivity, and they are described by a CTRW model for the Lagrangian particle dynamics. These results shed light on the structure of Lagrangian dynamics in complex media, and they provide insight for the upscaling of transport from the pore to the continuum scale. Next to the local organization of pores and their connectivity, longer conduits of fast velocity, so-called preferential flow paths, may introduce heterogeneity at larger scales that potentially influence transport significantly. We shall investigate this

further in a followup study in which different packs featuring a different pore structure will be compared with each other.

## ACKNOWLEDGMENTS

We acknowledge the contributions of R. Gallus and D. Sägesser in the frame of a laboratory project, U. Gülan for help with data processing, and W. Kinzelbach, T. LeBorgne, P. De Anna, and P.K. Kang for stimulating discussions. Financial support is acknowledged from the Swiss National Science Foundation (SNF Grant No. 144645) for M.H., Marie Curie International Incoming Fellowships (FP7-PEOPLE-2012-SoilArchnAg No. 302251) for V.L.M, and the European Research Council (ERC project MHetScale No. 617511) for M.D.

[1] L. Biferale, G. Boffetta, A. Celani, B. J. Devenish, A. Lanotte, and F. Toschi, Phys. Rev. Lett. **93**, 064502 (2004).
[2] R. Friedrich, J. Peinke, M. Sahimi, and M. Reza Rahimi Tabar, Phys. Rep. **506**, 87 (2011).
[3] F. Toschi and E. Bodenschatz, Annu. Rev. Fluid Mech. **41**, 375 (2009).
[4] P. de Anna, T. Le Borgne, M. Dentz, A. M. Tartakovsky, D. Bolster, and P. Davy, Phys. Rev. Lett. **110**, 184502 (2013).
[5] T. Le Borgne, M. Dentz, and J. Carrera, Phys. Rev. Lett. **101**, 090601 (2008).
[6] D. Kelley and N. Ouellette, Sci. Rep. **3**, 1073 (2013).
[7] D. Kramer and R. McLaughlin, Am. Zool. **41**, 137 (2001).
[8] J. Bear, *Dynamics of Fluids in Porous Media* (American Elsevier, New York, 1972).
[9] A. Tartakovsky, D. Tartakovsky, and P. Meakin, Phys. Rev. Lett. **101**, 044502 (2008).
[10] I. Mankel *et al.*, Appl. Phys. Lett. **90**, 174105 (2007).
[11] E. Codling, M. Plank, and S. Benhamou, J. R. Soc. Interface **5**, 813 (2008).
[12] D. R. Lester, G. Metcalfe, and M. G. Trefry, Phys. Rev. Lett. **111**, 174101 (2013).
[13] T. Le Borgne, M. Dentz, and E. Villermaux, Phys. Rev. Lett. **110**, 204501 (2013).
[14] V. Morales, J.-Y. Parlange, and T. Steenhuis, J. Hydrol. **393**, 29 (2010).
[15] J. D. Seymour, J. P. Gage, S. L. Codd, and R. Gerlach, Phys. Rev. Lett. **93**, 198103 (2004).
[16] M. Dentz, T. Le Borgne, A. Englert, and B. Bijeljic, J. Contam. Hydrol. **120-121**, 1 (2011).
[17] I. Battiato, D. Tartakovsky, A. Tartakovsky, and T. Scheibe, Adv. Water Resour. **32**, 1664 (2009).
[18] J. P. Bouchaud and A. Georges, Phys. Rep. **195**, 127 (1990).
[19] B. Berkowitz, A. Cortis, M. Dentz, and H. Scher, Rev. Geophys. **44**, RG2003 (2006).
[20] A. La Porta, G. Voth, A. Crawford, J. Alexander, and E. Bodenschatz, Nature (London) **409**, 1017 (2001).
[21] N. Mordant, A. M. Crawford, and E. Bodenschatz, Phys. Rev. Lett. **93**, 214501 (2004).
[22] S. Saleh, J. Thovert, and P. Adler, AIChE J. **39**, 1765 (1993).
[23] A. Cenedese and P. Viotti, Water Resour. Res. **32**, 2329 (1996).
[24] Y. Hassan and E. Dominguez-Ontiveros, Nucl. Eng. Design **238**, 3080 (2008).
[25] A. Huang, M. Huang, H. Capart, and R.-H. Chen, Exp. Fluids **45**, 309 (2008).
[26] D. Butscher, C. Hutter, S. Kuhn, and P. von Rohr, Exp. Fluids **53**, 1123 (2012).
[27] Y. Kutsovsky, L. Scriven, H. Davis, and B. Hammer, Phys. Fluids **8**, 863 (1996).
[28] L. Lebon, L. Oger, J. Leblond, J. Hulin, N. Martys, and L. Schwartz, Phys. Fluids **8**, 293 (1996).
[29] S. S. Datta, H. Chiang, T. S. Ramakrishnan, and D. A. Weitz, Phys. Rev. Lett. **111**, 064501 (2013).
[30] C. Scholz, F. Wirner, Y. Li, and C. Bechinger, Exp. Fluids **53**, 1327 (2012).
[31] K. Hoyer *et al.*, Exp. Fluids **39**, 923 (2005).
[32] B. Lüthi, A. Tsinober, and W. Kinzelbach, J. Fluid Mech. **528**, 87 (2005).
[33] M. Holzner and B. Lüthi, Phys. Rev. Lett. **106**, 134503 (2011).
[34] F. J. Pérez-Reche, S. N. Taraskin, W. Otten, M. P. Viana, L. da F. Costa, and C. A. Gilligan, Phys. Rev. Lett. **109**, 098102 (2012).
[35] M. Siena, M. Riva, J. D. Hyman, C. L. Winter, and A. Guadagnini, Phys. Rev. E **89**, 013018 (2014).
[36] A. D. Araújo, W. B. Bastos, J. S. Andrade, Jr., and H. J. Herrmann, Phys. Rev. E **74**, 010401(R) (2006).
[37] U. M. Scheven, D. Verganelakis, R. Harris, M. L. Johns, and L. F. Gladden, Phys. Fluids **17**, 117107 (2005).
[38] B. F. Bijeljic, A. Raeini, P. Mostaghimi, and M. J. Blunt, Phys. Rev. E **87**, 013011 (2013).
[39] P. K. Kang, P. de Anna, J. P. Nunes, B. Bijeljic, M. Blunt, and R. Juanes, Geophys. Res. Lett. **41**, 6184 (2014).
[40] M. Abramowitz and I. Stegun, *Handbook of Mathematical Functions* (Dover, New York, 1972).
[41] M. Moroni and J. Cushman, Water Resour. Res. **37**, 873 (2001).
[42] N. Goldenfeld and L. P. Kadanoff, Science **284**, 87 (1999).